Uplink Performance Analysis of Heterogeneous Non-Terrestrial Networks in Harsh Environments: A Novel Stochastic Geometry Model

Wen-Yu Dong, *Student Member, IEEE*, Shaoshi Yang, *Senior Member, IEEE*, Sheng Chen, *Life Fellow, IEEE*

***Abstract*—In harsh environments, such as mountainous terrain, dense vegetation and urban landscapes, a single type of unmanned aerial vehicles (UAVs) may encounter challenges like flight restrictions, difficulty in task execution or increased risk. Therefore, employing multiple types of UAVs to collaborate along with satellite assistance, becomes essential in such scenarios. In this context, we present a stochastic geometry based approach for modeling the heterogeneous non-terrestrial networks (NTNs) by using the classical binomial point process and introducing a novel point process, called Matérn hard-core cluster process (MHCCP) which possesses both properties of exclusivity and clustering. Through simulations, MHCCP has been validated as a more suitable model for UAV groups composed of multiple clusters, compared with traditional point processes such as Poisson point process, binomial point process, and Poisson cluster process. This is because MHCCP ensures inter-cluster repulsion while effectively capturing the clustered distribution observed in practical scenarios. Then, taking into account the influence of terrain shadows on the aerial-satellite links in low-altitude harsh environments, we derive closed-form expressions of the outage probability and average ergodic rate for the aerial-to-satellite uplink of heterogeneous NTNs. Unlike existing studies, our analysis adopts an advanced system configuration that combines beamforming with frequency division multiple access and incorporates a shadowed-Rician fading model to accurately capture signal fading under complex environmental conditions. Furthermore, we investigate link performance in the presence of co-channel interference. Monte Carlo simulations validate that the derived closed-form solutions of the outage probability and the average ergodic rate provide a precise quantitative tool for evaluating the reliability and transmission efficiency of the aerial-satellite links, offering deeper insights into system performance in complex environments.**

***Index Terms*—Heterogeneous non-terrestrial network, stochastic geometry, Matérn hard-core cluster process, binomial point process, outage probability, average ergodic rate**

I. Introduction

NON-TERRESTRIAL networks (NTNs), which include unmanned aerial vehicles (UAVs), high-altitude platforms and satellite networks, are extensively utilized for a myriad of purposes, such as remote sensing, navigation, disaster management and various commercial applications [1, 2]. In challenging environments, including disaster relief, complex terrain monitoring, and urban security and surveillance, single-type low-altitude UAV groups often encounter significant limitations. These UAVs often struggle to meet simultaneous demands for extensive coverage, endurance, anti-interference capabilities, and handling complex tasks. Moreover, difficult terrains such as mountainous regions, densely vegetated areas, or urban landscapes pose flight restrictions and task execution challenges, where specific UAV types may perform better under particular conditions. To address these challenges, heterogeneous UAV groups, composed of various UAV types with complementary strengths, become essential. This approach not only enhances operational capabilities and reliability but also ensures that UAV-based applications can adapt effectively to a wide range of complex and demanding scenarios. Furthermore, studying the performance of heterogeneous UAVs will offer valuable insights for designing and developing future UAV systems, ensuring their adaptability and resilience in dynamic, challenging environments.

In complex terrains, shadow fading caused by obstructions such as buildings, trees, and mountains significantly challenges the applicability of traditional fading models like Rayleigh, Rician, and Nakagami. The analysis becomes even more intricate in heterogeneous NTNs, where multiple UAV types, their spatial distributions, and varying communication characteristics add layers of complexity. Conventional methods, often reliant on discrete event simulations or network simulators [3, 4], provide insights but lack the mathematical rigor needed for a deeper understanding of network features. Additionally, these methods may face limitations when applied to specific network scenarios. To overcome these challenges, recent research has demonstrated the potential of stochastic geometry [5] and random geometric graphs [6] as effective analytical tools, offering new perspectives on network behavior and performance.

A. Related Works

Hybrid satellite-aerial-terrestrial networks (SATNs) have gained increasing attention as a key aspect of 6G, driven by the growing need for seamless global connectivity and advancements in this integrated communication paradigm.

This work was supported in part by Beijing Municipal Natural Science Foundation under Grant L242013; and in part by the Open Project Program of the Key Laboratory of Mathematics and Information Networks, Ministry of Education, China, under Grant KF202301. This work was presented in part at the IEEE Global Communications Conference, Cape Town, South Africa, Dec. 8-12, 2024. *(Corresponding author: Shaoshi Yang.)*

Wen-Yu Dong and Shaoshi Yang are with the School of Information and Communication Engineering, Beijing University of Posts and Telecommunications, Beijing 100876, China, also with the Key Laboratory of Universal Wireless Communications, Ministry of Education, Beijing 100876, China, and also with the Key Laboratory of Mathematics and Information Networks, Ministry of Education, Beijing 100876, China (e-mail: wenyu.dong@bupt.edu.cn, shaoshi.yang@bupt.edu.cn).

Sheng Chen is with the School of Electronics and Computer Science, University of Southampton, SO17 1BJ Southampton, U.K. (e-mail: sqc@ecs.soton.ac.uk).

Stochastic geometry has emerged as a powerful mathematical tool for addressing the challenges posed by SATNs, enabling the analysis of average network performance and offering valuable insights into network operations [7–17]. For example, [7] utilized stochastic geometry to analyze downlink performance and determine the effective number of satellites required for real-world networks with uneven satellite distributions across different latitudes. In addition, the researches conducted in [13–16] explored the downlink performance of a low Earth orbit (LEO) satellite communication system, by considering various fading channel models and satellite distribution models. The works [8, 12] on the other hand carried out uplink performance analysis for integrated SATNs, by focusing on the Rayleigh fading model in general situations and the empirical fading model in an urban setting. The paper [9] investigated the performance of cache-enabled SATNs, utilizing the non-orthogonal multiple access (NOMA) scheme, while the paper [10] focused on the analysis of end-to-end (e2e) performance in a cooperative SATN, considering either the satellite or the aerial relay. The authors of [11] specifically investigated the probability of establishing an end-to-end path from ground users to a satellite, considering scenarios both with and without aerial nodes serving as relays, and focused on spherical stochastic geometry analysis under Nakagami fading. The authors of [17] utilized a decode-and-forward relay method to establish a model for the cooperative SATN system and studied e2e outage probability (OP). However, all the aforementioned UAV systems are homogenous as they only consider single-type UAV. To date, few studies have focused on heterogeneous NTN systems involving two or more types of UAVs, primarily due to the increased complexity of the analysis process for such systems. Building on the foundational work on multi-layer LEO systems [18], our objective is to address the challenge of analyzing the uplink involving heterogeneous UAV groups. Besides, the interference which has significant impact on the system performance in a wireless network with numerous concurrent transmissions is often overlooked in the various existing studies [13–17], as its exclusion simplifies the analysis and derivation process. Addressing this interference issue is therefore another key focus of our research.

Most of the above works conducted the modeling using Poisson point process (PPP) and/or Poisson cluster process (PCP), which are well known for their mathematical tractability. Specifically, it is convenient to use them in deriving the performance of a network where the node density is known and the number of nodes in different disjoint subareas is independent. However, they are not suitable for modeling the nonstationary and often nonisotropic distribution in a finite-area network with a fixed number of nodes, where the number of nodes is also not independent among different disjoint regions [19, 20]. The same issue also arises with a special type of PCP, namely Matérn cluster process (MCP) [21], as the parent points in MCP are constructed based on the rules of PPP. On the other hand, since both Matérn hard-core point process (MHCPP) [22] and binomial point process (BPP) are defined within finite regions, they can be naturally adopted to size-limited areas with spatial boundaries, which means that the utilization of them are deemed more suitable in this particular scenario for elucidating the attributes of the network configuration. Furthermore, due to its exclusionary nature, MHCPP is well-suited for modeling UAVs that need to maintain a certain safe distance from each other. However, traditional MHCPP cannot capture the characteristics of clustered tasks for UAVs. Thus, we need a point process that combines both exclusion and clustering properties for heterogeneous NTN systems.

In contrast to Rayleigh and Nakagami-m fading, shadowed-Rician (SR) fading [23] has been proven to be more appropriate for the statistical characterization of satellite channels. This model has been found to be applicable across several frequency bands, such as S-, L-, Ku-, and Ka-band, making it a versatile choice for modeling satellite communication channels. While the SR model is extensively employed in satellite link research, system-level analysis is understudied. With LEO satellites located at different altitudes, the work [13] investigated the joint coverage probability from satellites to satellite gateways in remote areas and then to anchor base stations, given that the satellite-to-gateway link is subject to SR fading. The authors of [24] derived the downlink OP of the LEO satellite communication system under SR fading based on a BPP distribution and optimized the system throughput under visibility and outage constraints. Nevertheless, similar to majority of the works utilizing SR models, these two papers solely examined SNR while neglecting the consideration of interference. In recent studies on uplink communications with SINR, [25] employed the Gaussian mixture model (GMM) for channel fading, rather than the SR model. On the other hand, in studies [26–29] that used the SR model and incorporated SINR, the SR model was approximated using the Gamma function. Song *et al.* [10] employed the Nakagami-m fading model rather than the SR fading model for the purpose of estimating statistical values of interference. Hence, it is evident that the interference analysis with the SR model remains unexplored. In our previous work [30], we have partially explored this aspect; however, it lacks a detailed analysis of the proposed novel point process and an in-depth investigation of different performance metrics based on the SR fading.

B. Contributions and Organization of the Paper

Motivated by the aforementioned discoveries, this study investigates the heterogeneous NTN system, comprising two distinct groups of UAVs and one satellite. To better model such a heterogeneous NTN, we introduce a novel point model called Matérn hard-core cluster process (MHCCP)[1]. The location distributions of these two UAV groups are described as the MHCCP for one group and the BPP for the other group. Furthermore, beamforming and frequency division multiple access (FDMA) are employed to improve network efficiency. Since in this heterogeneous NTN system, nodes operating within the same subchannel share the same frequency band, we explicitly investigate the effects of multi-user interference

[1]MHCCP is a point process that combines clustering behavior with spatial exclusion by introducing a hard-core distance, which ensures a minimum separation between cluster heads while allowing other points to cluster around them within a defined radius. The specific construction rules will be provided in the system model section.

TABLE I
COMPARISON OF EXISTING STATE-OF-THE-ARTS FOR SATELLITE RELATED NETWORKS WITH OUR PROPOSED WORK

Reference	Link types	Channel fading model of target signal	Channel fading model of interference signal	Multi-access	Beamforming	Point process
Zhang *et al.* [9]	S-A-T	S-A: SR A-T: Nakagami	-	NOMA	-	PCP
Song *et al.* [10]	A-S-T	A-S: Nakagami S-T: SR	Nakagami	CDMA	-	MHCPP/PPP
Liu *et al.* [11]	T-A-S/T-S	Nakagami	Nakagami	FDMA	-	PCP/PPP
Al-Houraniet *al.* [12]	T-S	Empirical Model	Empirical Model	-	-	PPP
Talgat *et al.* [13]	S-GW-U	S-GW: SR GW-U: Rayleigh	-	-	-	BPP/PPP
Al-Houraniet *al.* [14]	S-T	GMM	-	-	-	PPP
Okatiet *al.* [15]	S-T	Rayleigh	-	-	-	NPPP
Zhang *et al.* [17]	S-A-T	SR	-	Single-User	-	Single-Point
Jung *et al.* [24]	S-T	SR	-	-	-	BPP
Al-Houraniet *al.* [25]	T-S	GMM	GMM	-	-	BPP
Jia *et al.* [26]	T-S	SR (Approximating to a Gamma function)	SR (Approximating to a Gamma function)	-	-	PPP
Sellathurai *et al.* [27]	S-T	SR (Approximating to a Gamma function)	SR (Approximating to a Gamma function)	-	-	PPP
Kolawole *et al.* [28]	S-U/GW-U	S-U: SR (Approximating to a Gamma function) T-U: Nakagami	Nakagami	-	✓	PPP
Talgat *et al.* [29]	T-S/T-GW-S	T-S: SR (Approximating to a Gamma function) T-GW-S: Rayleigh	T-S: SR (Approximating to a Gamma function) T-GW-S: Rayleigh	-	-	BPP/PCP
Our work	A-S	SR	SR	FDMA	✓	MHCCP/BPP

S: satellite, A: aerial node, T: terrestrial node, GW: gateway, U: ground user node. SR: shadowed-Rician fading, GMM: Gaussian mixture model. ✓: considered, - : not considered. PCP: Poisson cluster process (contains Matérn cluster process and Tomas cluster process), MHCPP: Matérn hard-core point process, PPP: Poisson point process, NPPP: nonhomogeneous Poisson point process, BPP: binomial point process, MHCCP: Matérn hard-core cluster process.

(MUI) under SR fading channels. Our contributions can be summarized as follows.

- Unlike existing studies that often simplify system models, we adopt a more realistic approach to analyzing the performance of heterogeneous NTNs by considering key factors such as network deployment, multi-access mechanisms, beamforming models, and channel characteristics. Specifically, we integrate beamforming, FDMA, and heterogeneous UAVs with different point distribution models into the aeronautical communication system, focusing on evaluating how these techniques impact link quality.
- While many existing studies overlook interference analysis, we account for interference in the presence of SR fading when analyzing uplink performance in heterogeneous NTNs. Although the SR fading model provides a more accurate depiction of the aerospace channel, it introduces challenges in interference analysis. We overcome these challenges by deriving a detailed solution for the statistical analysis of MUI within the fading model used in satellite communications.
- Building on existing point models, we modify the type-II MHCPP to better accommodate the clustering scenario for UAV modeling. The resulting point process, MHCCP, combines both clustering and exclusion characteristics, ensuring uniform dispersion of cluster members within the exclusion region, and enabling tasks to be performed at the cluster level. Due to the repulsion effect, MHCCP has an upper density limit, distinguishing it from the properties of MCP and PPP models. The impact of density on the number of nodes in MHCCP is derived and validated through both theoretical analysis and numerical simulations.
- Our uplink performance analysis for heterogeneous NTNs is highly accurate, with theoretical results validated through Monte Carlo simulations. Specifically, we derive precise mathematical formulations for the OP and the average ergodic rate (AER) of a designated transmitter within the heterogeneous NTN. Additionally, we provide detailed numerical results for these two connectivity metrics and analyze the impact of key system parameters, such as the target transmitter's power, the size of the point distribution space, the node density, the transmission distance, and the number of frequency channels.

Table I compares our work with some state-of-the-art contributions related to satellite networks, in order to highlight the novelty of our contributions.

The remainder of this paper is organized as follows. In Section II, the topology model, the channel model, and the SINR model of a heterogeneous NTN are presented. Section III provides our primary performance analysis results, which involve the derivation of the analytical uplink OP and AER of an aerial transmitter. An investigation of the Laplace transform of interference power is also included. In Section IV, we provide numerical results to verify our theoretical derivations and to study the effect of key system parameters, such as network scale, the number of orthogonal frequency channels in the constellation and the constellation altitude as well as the channel parameters, on the network performance. Our conclusions are drawn in Section V.

Notation: $\mathbb{P}(\cdot)$ indicates the probability measure and $\mathbb{E}[\cdot]$

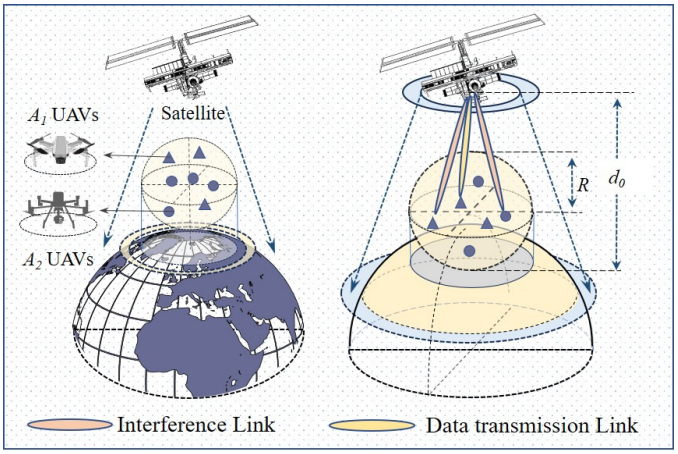

Fig. 1. Illustration of the heterogeneous NTN system.

indicates the average measure. The Laplace transform of random variable X is defined by $\mathcal{L}_X(s) = \mathbb{E}\left[\exp(-sX)\right]$. The cumulative distribution function (CDF) and probability density function (PDF) of random variable X are denoted by $F_X(x)$ and $f_x(x)$, respectively. $\Gamma(\cdot)$ is the Gamma function, and the Pochhammer symbol is defined as $\mathrm{Ps}(x)_n = \Gamma(x+n)/\Gamma(x)$. The lower incomplete Gamma function is defined as $\gamma(a,x) = \int_0^x t^{a-1}\exp(-t)dt$. $\binom{n}{k}$ denotes the binomial coefficient. ${}_1F_1\left(\cdot;\cdot;\cdot\right)$ is the confluent hypergeometric function of the first kind. The mathematical notations adopted in this paper are summarized in Table II.

II. System Model

We consider an NTN composed of an LEO satellite S and two heterogeneous UAV groups, A_1 and A_2, as illustrated in Fig. 1. These UAV groups exhibit distinct characteristics in terms of deployment and transmitter capabilities.

For example, in tasks such as geological disaster detection or post-disaster rescue, UAV group A_1 operates in clustered formations to efficiently survey surface areas. In contrast, UAV group A_2 functions independently, providing the flexibility to navigate challenging terrains such as canyons, mountainous regions, or indoor structures for localized monitoring and reconnaissance. The trajectories of LEO satellites are predictable, and their receiver antennas are designed with a wide coverage angle, ensuring effective communication over large areas. We also assume that the impact of Doppler shifts caused by the high-speed movement of LEO satellites and the low-speed movement of UAVs can be effectively mitigated by invoking accurate estimation and compensation techniques[2]. Our analysis focuses on the uplink connection between UAV groups and a specific satellite.

TABLE II
Summary of Mathematical Notations Adopted.

Notation	Description
A_1; A_2	Two types of UAV groups
Φ_{A_1}	Point set composed of nodes in A_1
Φ_{A_2}	Point set composed of nodes in A_2
Φ_c	Point set of parent points following MHCPP
λ_1	Density of candidate points
λ_2	Density of parent points
λ_3	Density of Φ_{A_2}
N_1	Total number of nodes in A_1
N_2	Total number of nodes in A_2
K	Number of frequency channels
D	Distance between two candidate points
$D_{\min}$	Minimum distance between two candidate points
G_{t}	Array gain of main lobes
g_{t}	Array gain of side lobes
P_{out}	Outage probability
$\bar{C}$	Average ergodic rate
$\mathcal{V}$	Space for deployment of all air nodes
$\bar{c}$	Parameter of MCP
α	Path-loss exponent
T	SINR threshold for outage probability
σ^2	AWGN's power spectral density

A. Topology Model

1) Deployment of A_1 and A_2: As noted in [19, 20], accurately modeling networks with a finite number of nodes and a limited area using a PPP is impractical. Without loss of generality, the aerial transmitters are assumed to be randomly deployed in a spherical space. Considering that the radius of UAV coverage areas is much smaller than the distances from UAVs to the satellite, we opt to model both A_1 and A_2 within the same spherical space for the sake of simplicity. In fact, regardless of whether the two heterogeneous UAV groups are within the same spherical space, their distance distribution to the satellite remains unaffected by this assumption, which in turn does not affect the derived results. In practical applications, A_1 typically consists of a finite number of nodes and operates within a region of limited size. Therefore, its distribution is modeled as a Binomial Point Process (BPP), denoted as Φ_{A_1}, with N_1 representing the number of nodes within a spherical region $\mathcal{V}$ of radius R. For A_2, the MHCCP framework is used to model its clustered networking structure, ensuring a minimum separation distance between clusters. Fig. 2 illustrates the node distribution for A_1 and A_2.

2) Construction of MHCCP: Constructing an MHCCP begins with sparsifying a PPP through the application of a hard-core distance, which removes certain points to ensure a minimum separation between them. The points obtained after carrying out the above operations become cluster heads, each defining a cluster where members are distributed within half the hard-core distance around head. This approach generates a new point process in which the hard-core distance between clusters prevents overlap, ensuring clear separation. Consequently, MHCCP achieves both spatial clustering of points and regulated separation between clusters, effectively integrating clustering behavior with spatial exclusion principles. We then outline the three-step process for constructing the MHCCP, denoted as Φ_{A_2}.

In the first step, candidate points are uniformly generated within the spherical space $\mathcal{V}$ using a homogeneous PPP with

[2]For dealing with the Doppler shifts caused by satellite movement, these techniques rely on detailed satellite ephemeris data, including orbit type, altitude, position, and velocity, which are used to accurately predict and compensate for frequency shifts in advance [31, 32]. For UAVs, their low-altitude and low-speed characteristics make Doppler shifts relatively minor. Additionally, since the motion models of individual UAVs are well-defined, these shifts can be effectively estimated and compensated, either through onboard processing or external control systems.

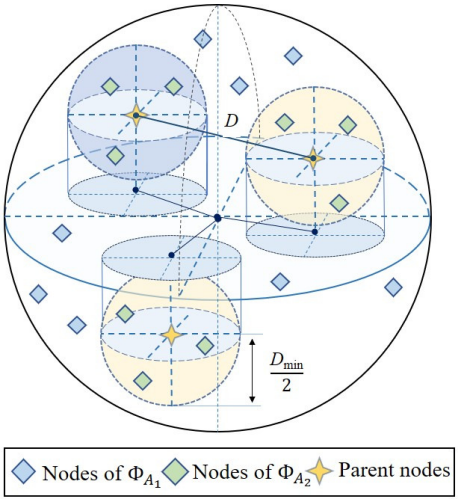

Fig. 2. Illustration of node positions in heterogeneous UAV network.

density λ_1. The spherical space has a radius R_1 and a volume V_1. The number of candidate points, denoted as N_c, follows a Poisson distribution. The probability mass function of N_c is given by $\mathbb{P}(N_c = s) = \frac{\lambda_1 V_1}{s!}\exp(-\lambda_1 V_1)$, where s represents the number of candidate points.

In the second step, each candidate point is assigned with an independent mark, randomly drawn from a uniform distribution within the range $[0,\ 1]$. Subsequently, we exclusively retain the point with the smallest mark within a confined spherical space with the radius $D_{\min}$ by eliminating the others. Specifically, for a given point Q serving as the center of a spherical exclusion zone with the radius $D_{\min}$, any other candidate points within this zone are compared by their mark values, and only the point with the smallest mark is retained. This process is repeated iteratively for each candidate point until every exclusion zone contains exactly one point. As a result of this elimination process, the distance D between any two retained points is guaranteed to be at least $D_{\min}$. The resulting hard-core point process, denoted as Φ_c, has a density λ_2, which can be expressed mathematically as: $\lambda_2 = \frac{1-\exp(-\frac{4}{3}\pi D_{\min}^3 \lambda_1)}{\frac{4}{3}\pi D_{\min}^3}$.

In the final step, the points in Φ_c are treated as parent points, and subpoints are uniformly generated within spheres of radius $D_{\min}/2$ centered on each parent point. The subpoints are distributed according to a BPP with parameter $\bar{c}$, where $\bar{c}$ represents the number of members in each cluster of A_2. This clustering process completes the construction of the MHCCP, with Φ_{A_2} comprising all the generated subpoints. Consequently, the set of points Φ_{A_2} in A_2 follows the MHCCP. The relationship between the density of the parent points λ_2 and the density of Φ_{A_2}, denoted as λ_3, is given by $\lambda_3 = \lambda_2 \bar{c}$, and hence

$$\lambda_3 = \bar{c}\frac{1 - \exp(-\frac{4}{3}\pi D_{\min}^3 \lambda_1)}{\frac{4}{3}\pi D_{\min}^3}. \tag{1}$$

B. Point Process Characteristics

Mathematical methods for analyzing differences or similarities between point patterns rely on key characteristics of point processes. One commonly used tool in the statistical analysis of spatial point patterns is the pair correlation function (PCF), a second-order function based on inter-point distance r. The PCF characterizes interactions between points at varying distances, revealing whether they exhibit attraction (clustering), repulsion, or neutrality. By leveraging this function, we can both qualitatively explore the spatial structure of point patterns and quantitatively assess these structures over specific distance ranges, providing a more precise understanding of the underlying spatial relationships.

1) Pair correlation function: The PCF, denoted as $g(r)$, provides information about the relative frequency of point pairs separated by a specific distance r. Specifically, it measures the relative density of point pairs at distance r, normalized against the expected density under complete spatial randomness (CSR). Under CSR, where points are independently and uniformly distributed, the PCF satisfies $g(r) = 1$ for all values of r. Deviations from this baseline indicate spatial interactions: $g(r) > 1$ suggests clustering of point pairs at distance r, while $g(r) < 1$ implies repulsion. By definition, the PCF is mathematically expressed as:

$$g(r) = \frac{\mathrm{d}K(r)}{4\pi r^2 \lambda \mathrm{d}r}, \tag{2}$$

where λ is the overall density of the point process, and $K(r)$ is the Ripley's K-function.

The formula of the Ripley's K-function is as follows:

$$K(r) = \frac{V}{n^2}\sum_{i=1}^{n}\sum_{j=1}^{n}\frac{I_r(t_{ij})}{w_{ij}}(i \neq j), \tag{3}$$

where V is the volume of the region to be studied, n is the total number of points in the point pattern, t_{ij} is the Euclidean distance between points i and j, $I_r(t_{ij})$ is an indicator function that equals 1 if the distance $t_{ij} \leq r$, and 0 otherwise. In addition, w_{ij} is a weighting factor to account for edge effects (i.e., boundary correction), and it is typically used when points are close to the boundaries of the region to be studied.

2) Comparison of Characteristics of Different Point Processes: To highlight the unique characteristics of our proposed MHCCP, we compare it with three classic point processes: MCP, PPP, and BPP.

Fig. 3 provides three-dimensional visualizations of the point distributions for these four point processes, with gray spheres representing the cluster boundaries. A closer examination reveals that clusters in MCP exhibit significant overlap, while MHCCP demonstrates distinct inter-cluster repulsion. This distinction underscores the dual properties of MHCCP, which combines clustering behavior with inter-cluster repulsion. In contrast, BPP and PPP lack clustering characteristics, further emphasizing the distinctive nature of MHCCP.

Fig. 4 depicts the PCF $g(r)$. For small values of r, the PCF curves for both MHCCP and MCP rise significantly above 1, reflecting strong clustering effects in these point processes. At larger values of r, however, the PCF of MHCCP drops below 1, indicating inter-cluster repulsion, as previously observed. In contrast, the PCF of MCP approaches 1 at larger distances, suggesting the absence of such repulsion. Meanwhile, the PCF curves for PPP and BPP remain near 1 across all distances,

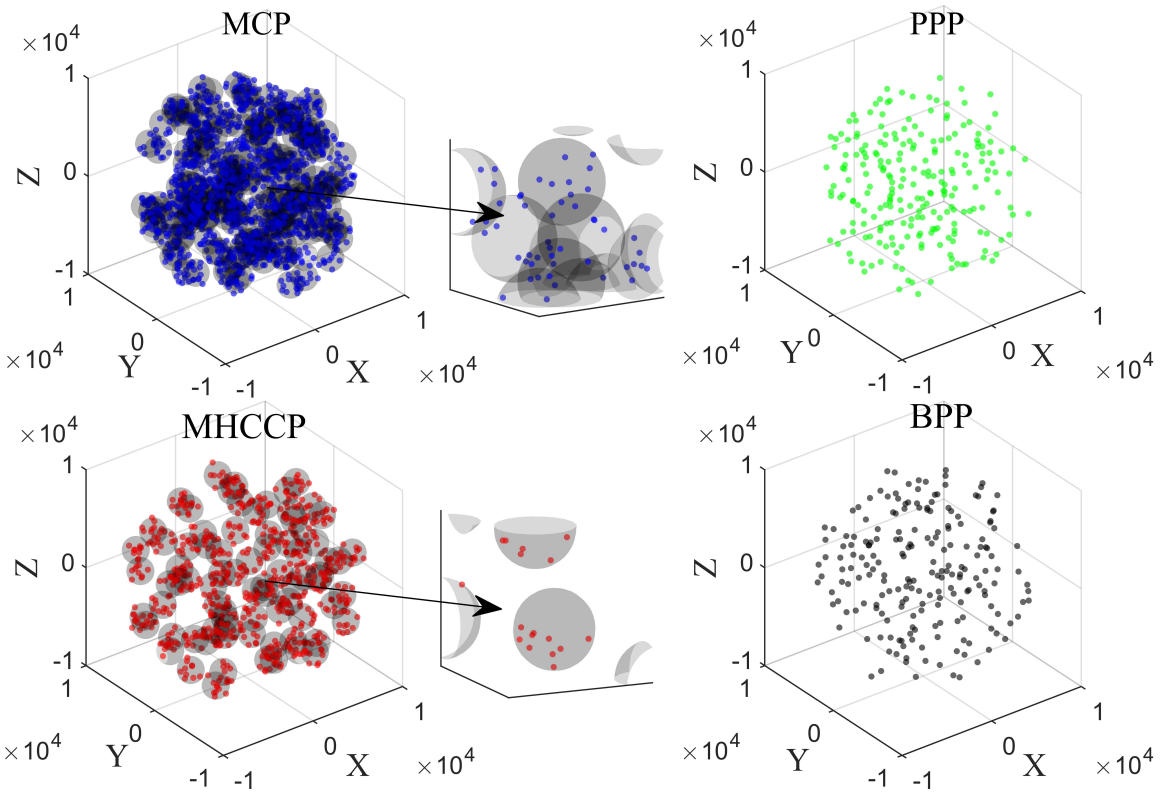

Fig. 3. 3D illustration of the point distribution of MHCCP, MCP, PPP and BPP.

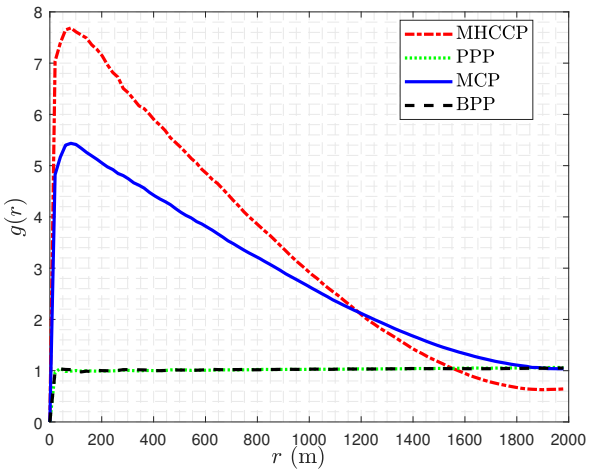

Fig. 4. PCF of MHCCP, MCP, PPP and BPP.

indicating that points in these processes are independent and exhibit neither clustering nor repulsion.

C. Channel Model and Access Mechanisms

1) Directional Beamforming Modeling: To enhance the strength of the received signal and optimize transmission performance, directional beamforming is employed at aerial transmitters and satellite receivers. For simplified processing, the actual antenna is modeled as a sector antenna. Given the satellite's extensive coverage capabilities, it is reasonable to assume that the satellite receiver can effectively capture UAV signals through the main lobe. Let i be the index of a specific link, l represent the index of a UAV group in A_1 or A_2, m be the target node, and x_l the interference node of the l-th UAV group. The overall directional gain of link i is denoted as D_i, where sub-indexes t and r refer to the transmitter and receiver, respectively. In this context, $G_{\rm t}$ and $g_{\rm t}$ represent the transmitter's main and side lobe gains,while the angular width of the transmitter's main lobe is denoted by θ. Similarly, $G_{\rm r}$ represents the main lobe gain of the receiver array.

Hence the value of D_m for the link from a given target node m to the satellite receiver is equal to $D_m = G_{\rm t}G_{\rm r}$. On the other hand, the value of D_{x_l} for any other interference node x_l is determined by the directivity gains of the main and side lobes of the antenna beam pattern. Accordingly, the probability distribution of D_{x_l} is expressed as:

$$D_{x_l} = \begin{cases} G_{\rm t}G_{\rm r}, & {\rm P}_{\rm M,M} = \frac{\theta}{2\pi}, \\ g_{\rm t}G_{\rm r}, & {\rm P}_{\rm S,M} = 1 - \frac{\theta}{2\pi}, \end{cases} \tag{4}$$

where the indexes M and S denote the main and side lobes, respectively, and ${\rm P}_{t,{\rm M}}$, $t \in \{{\rm M}, {\rm S}\}$, denotes the probability of the link in state $\{t, {\rm M}\}$.

2) Channel Fading: The SR fading model [33] is commonly utilized in satellite-terrestrial links on a range of frequency bands, such as S and Ka-bands, for both fixed and mobile satellite services [34], [35]. For the heterogeneous NTN studied in this paper, the presence of abundant shadows due to complex terrain, along with the predominant propagation path being the line-of-sight (LoS) path, closely aligns with the characteristics of SR fading. Therefore, utilizing SR fading for modeling the aerial-satellite link in complex terrain at low altitudes is reasonable. The SR fading model encompasses both the LoS component and the scatter component. We define $2c$ as the mean power of the multi-path component excluding

the LoS component, Ω as the average power of the LoS component, and q as the Nakagami-m fading parameter. The small-scale fading is denoted by $|h|^2$. The PDF of $|h|^2$ can be mathematically stated as [36]

$$f_{|h|^2}(x) = \kappa \exp(-\beta x)\, {}_1F_1(q;1;\delta x), \tag{5}$$

where $\kappa = \frac{(2cq)^q}{2c(2cq+\Omega)^q}$, $\delta = \frac{\Omega}{2c(2cq+\Omega)}$ and $\beta = \frac{1}{2c}$.

3) Multi-access Mechanism: Multi-access mechanisms in aerial-to-satellite communications play an important role in improving the uplink performance. To enhance the network's connectivity and capacity, the FDMA is employed, implementing frequency reuse across a total of K orthogonal frequency channels ($K \leq N_1$). N_2/K represents the number of UAVs competing for the same sub-band, which is designed to be an integer. In addition, we assume $N_2/K = k\bar{c}$, where k is also an integer and $\bar{c}$ is the number of UAVs in each cluster. This assumption indicates that multiple clusters, i.e., k clusters, can share the same sub-band. Similarly, the nodes in A_1 are divided into K subgroups, which collectively share the same spectrum resources as A_2. Consequently, each subgroup of N_1/K nodes in A_1 and N_2/K nodes in A_2 share the same sub-band. This implies that $N_1/K + N_2/K$ aerial transmitters operate on a common sub-band, inevitably resulting in co-channel interference. For analytical purposes, we randomly select one sub-band from the K available sub-bands and denote the sets of nodes from the two UAV groups sharing this common sub-band as Φ_1 and Φ_2, respectively, where we have $|\Phi_1| = N_1/K$ and $|\Phi_2| = N_2/K$. Focusing on the usage of a single sub-band allows for a clearer understanding of interference dynamics and performance evaluation under these shared spectrum conditions.

D. SINR Model

Based on the aforementioned model, the SINR, a metric for evaluating wireless link performance, can be expressed as:

$$\mathrm{SINR} = \frac{p_m D_m |h_m|^2 d_m^{-\alpha}}{I + \sigma^2}, \tag{6}$$

where I represents the interference experienced by the target node from other UAVs in the heterogeneous UAV groups, $I = \sum_{l\in\{1,2\}} \sum_{x_l \in \phi_l \setminus \{m\}} p_{x_l} D_{x_l} |h_{x_l}|^2 d_{x_l}^{-\alpha}$ with l being the index of a particular UAV group in A_1 and A_2, m is the target node, x_l is the interference node of the l-th UAV group, p_m and p_{x_l} are the transmit power at m and x_l, while d_m is the distance between m and the satellite, d_{x_l} is the distance between x_l and the satellite, α is the path-loss exponent, and σ^2 is the strength of additive white Gaussian noise (AWGN).

III. Performance Analysis

This section analyzes the OP and AER for the proposed heterogeneous NTN model. Specifically, we substitute the SINR from the system model into the defined expressions for OP and AER. A key step in this process involves deriving the Laplace transform of the interference, which is essential for obtaining the final closed-form expressions for OP and AER. Without loss of generality, we assume a uniform transmission power level for all transmitters within each UAV group, except for the target transmitter. In particular, the power of the target transmitter m is denoted as , while the transmission power levels for UAVs in the two groups, Φ_{A_1} and Φ_{A_2}, are denoted as p_1 and p_2, respectively.

A. Outage Probability

The OP represents the likelihood that the SINR at the receiver falls below a predefined threshold, indicating that the minimum SINR required for successful data transmission is not achieved. In this scenario, when the SINR is below the threshold T, the transmitter is considered to be outside the receiver's effective coverage.

As a critical reliability metric, the OP quantifies the probability of communication failure due to random and adverse channel conditions, such as deep fading, interference, or shadowing. By analyzing the OP, we gain insights into how often the system fails to meet the minimum quality of service (QoS) requirements under such conditions. In fading environments, the OP specifically captures the probability of the channel being in an "outage" state, reflecting the system's ability to maintain link connectivity under varying SINR levels.

For links between low-altitude UAVs and LEO satellites, where channel conditions are highly dynamic and unpredictable, the OP is essential for evaluating coverage reliability and the robustness of the communication link. It provides a measure of the system's resilience to link quality variations. The OP for such links is defined as follows:

$$P_{\mathrm{out}} \triangleq \mathbb{P}(\mathrm{SINR} \leq T) = \mathbb{P}\left(\frac{p_m D_m |h_m|^2 d_m^{-\alpha}}{I + \sigma^2} \leq T\right), \tag{7}$$

where T is the SINR threshold. The following theorem derives a useful expression for OP.

Theorem 1. *The outage probability for an arbitrarily located aerial node under the SR fading channel is given by*

$$P_{\mathrm{out}} = \sum_{k=0}^{\infty} \frac{\Psi(k)}{(\beta-\delta)^{k+1}} \Gamma(k+1) \sum_{t=0}^{k+1} \binom{k+1}{t} (-1)^t \times \mathbb{E}\left[\exp\left(-s(I+\sigma^2)\right)\right], \tag{8}$$

where $\Psi(k) = \frac{(-1)^k \kappa \delta^k}{(k!)^2} \mathrm{Ps}(1-q)_k$, $s = \frac{t\zeta(\beta-\delta)T d_m^{\alpha}}{p_m D_m}$ *and* $\zeta = (\Gamma(k+2))^{-\frac{1}{k+1}}$.

Proof. See Appendix A. □

In order to further simplify the expression, we express $\mathbb{E}\left[\exp(-s(I+\sigma^2))\right]$ as

$$\begin{aligned}\mathbb{E}\left[\exp(-s(I+\sigma^2))\right] &= \mathbb{E}\big[\exp(-s\sigma^2)\big]\, \mathbb{E}\big[\exp(-sI)\big] \\ &= \mathbb{E}_{d_m}\big[\exp(-s\sigma^2)\big]\, \mathbb{E}_{d_m, I}\big[\exp(-sI)\big].\end{aligned} \tag{9}$$

In (9), the average operation for the first component is over the random variable d_m, and the average operation for the second component is over both d_m and the interference I.

Given that the distances between aerial nodes in finite-area networks are typically limited to a few kilometers, while the distance to the satellite extends to the range of hundreds or even thousands of kilometers, it is reasonable to assert that the latter is significantly greater in magnitude than the former.

Therefore, it is assumed that all the aerial transmitters possess an equal transmission distance to the satellite, i.e., $d_m = d_{x_l} = d_0$. Consequently, we obtain

$$\mathbb{E}\left[\exp(-s(I+\sigma^2))\right] = \exp(-s\sigma^2)\mathcal{L}_I(s), \tag{10}$$

where $\mathcal{L}_I(s)$ is the Laplace transform of the cumulative interference power I that is expressed in Lemma 1.

Lemma 1. *The Laplace transform of random variable I is:*

$$\begin{aligned}\mathcal{L}_I(s) =& \mathbb{E}[\exp(-sI)] \\ =& \left(M_2(1)\right)^{n_1} \exp\left(\lambda_3 V_1 (M_2(2)-1)\right),\end{aligned} \tag{11}$$

where λ_3 is given in (1), and

$$V_1 = \frac{4\pi R_1^3}{3}, \tag{12}$$

$$M_2(l) = M_1(\mu_l)\frac{\theta}{2\pi} + M_1(\nu_l)\left(1-\frac{\theta}{2\pi}\right),\ l\in\{1,2\}, \tag{13}$$

with

$$M_1(t_l) = \frac{(2cq)^q(1+2ct_l)^{q-1}}{\left((2cq+\Omega)(1+2ct_l)-\Omega\right)^q},\ t_l \in \{\mu_l, \nu_l\}, \tag{14}$$

$$\mu_l = s p_l d_0^{-\alpha} G_{\mathrm{t}} G_{\mathrm{r}},\ l\in\{1,2\}, \tag{15}$$

$$\nu_l = s p_l d_0^{-\alpha} g_{\mathrm{t}} G_{\mathrm{r}},\ l\in\{1,2\}, \tag{16}$$

and when the target UAV node is in Φ_{A_1} or Φ_{A_2}, n_1 is given by $\frac{N_1}{K}-1$ and $\frac{N_1}{K}$, respectively.

Proof. See Appendix B. □

Remark 1. *According to Lemma 1, we can obtain the Laplace transform of interference. The MHCCP model exhibits strong repulsion between clusters, which is determined by the minimum distance separating them. Consequently, the system's total number of nodes cannot exhibit unlimited growth as λ_1 rises. In order to ascertain the upper limit of nodes in this system, we differentiate the function λ_3 over λ_1, yielding $\frac{\mathrm{d}\lambda_3}{\mathrm{d}\lambda_1} = \bar{c}\left(\frac{4}{3}\pi D_{\min}^3\right)^2 \exp\left(-\frac{4}{3}\pi D_{\min}^3\lambda_1\right)$. Notably, $\frac{\mathrm{d}\lambda_3}{\mathrm{d}\lambda_1} \geq 0$. Moreover, $\lim\limits_{\lambda_1\to\infty}\frac{\mathrm{d}\lambda_3}{\mathrm{d}\lambda_1} = 0$. Hence, the upper limit of λ_3 can be established as $\lim\limits_{\lambda_1\to\infty}\lambda_3 = \frac{3\bar{c}}{4\pi D_{\min}^3}$, whose validity will be further examined in the simulation discussed in Section IV.*

By substituting (10) and (11) into (8) and noting the definitions of (12) to (16), we derive the analytical closed-form expression for the OP, given in (17) at the bottom of this page.

B. Average Ergodic Rate

The AER, measured in bits/s/Hz and also known as Shannon throughput, represents the mean data rate that a communication system can achieve over time, normalized to unit bandwidth. It reflects the average performance of the system, considering the variations in the channel due to fading, as it computes the ergodic capacity based on the Shannon-Hartley theorem.

By averaging the achievable rates across all possible channel conditions, the AER provides an effective measure of the system's overall efficiency and data transmission capability. This metric is crucial, because it accounts for both short-term fluctuations and long-term trends in channel quality caused by phenomena such as multipath fading, interference, and shadowing. By capturing the statistical nature of the channel, the AER offers a realistic evaluation of sustained performance in dynamically changing environments, making it essential for optimizing resource allocation and ensuring efficient communication in practical systems. The definition of the AER is

$$\bar{C} \triangleq \mathbb{E}\left[\log_2\left(1+\mathrm{SINR}\right)\right]. \tag{18}$$

Theorem 2. *Under a SR fading serving channel, the average rate of any arbitrary UAV node is given by*

$$\begin{aligned}\bar{C} = \int_{t>0}\Bigg(1 - \sum_{k=0}^{\infty}\frac{\Psi(k)}{(\beta-\delta)^{k+1}}\Gamma(k+1)\sum_{j=0}^{k+1}\binom{k+1}{j}(-1)^j \\ \times \exp\left(-s\sigma^2\right)\left(M_2(1)\right)^{n_1}\exp\left(\lambda_3 V_1(M_2(2)-1)\right)\Bigg)\mathrm{d}t.\end{aligned} \tag{19}$$

Proof. See Appendix C. □

IV. Numerical Results

In this section, we validate the derived theoretical expressions by Monte-Carlo simulations. Unless otherwise explicitly

$$\begin{aligned}P_{\mathrm{out}} =& \sum_{k=0}^{\infty}\frac{\Psi(k)}{(\beta-\delta)^{k+1}}\Gamma(k+1)\sum_{t=0}^{k+1}\binom{k+1}{t}(-1)^t\exp\left(-s\sigma^2\right)\left(M_2(1)\right)^{n_1}\exp\left(\lambda_3 V_1(M_2(2)-1)\right) \\ =& \sum_{k=0}^{\infty}\frac{(-1)^k\kappa\delta^k\mathrm{Ps}(1-q)_k}{k!(\beta-\delta)^{k+1}}\sum_{t=0}^{k+1}\binom{k+1}{t}(-1)^t\exp\left(-\frac{t\zeta(\beta-\delta)Td_0^{\alpha}\sigma^2}{p_m D_m}\right) \\ &\times\left(\frac{(2cq)^q\left(1+\frac{2tcp_1G_{\mathrm{t}}G_{\mathrm{r}}\zeta(\beta-\delta)T}{p_mD_m}\right)^{q-1}}{\left((2cq+\Omega)\left(1+\frac{2tcp_1G_{\mathrm{t}}G_{\mathrm{r}}\zeta(\beta-\delta)T}{p_mD_m}\right)-\Omega\right)^q}\frac{\theta}{2\pi} + \frac{(2cq)^q\left(1+\frac{2tcp_2G_{\mathrm{t}}G_{\mathrm{r}}\zeta(\beta-\delta)T}{p_mD_m}\right)^{q-1}}{\left((2cq+\Omega)\left(1+\frac{2tcp_2G_{\mathrm{t}}G_{\mathrm{r}}\zeta(\beta-\delta)T}{p_mD_m}\right)-\Omega\right)^q}\left(1-\frac{\theta}{2\pi}\right)\right)^{n_1} \\ &\times\exp\left(3a\bar{c}V_1\left(1-\exp\left(-\frac{4}{3}\pi D_{\min}^3\lambda_1\right)\right)\left(\frac{(2cq)^q\left(1+\frac{2tcp_1g_{\mathrm{t}}G_{\mathrm{r}}\zeta(\beta-\delta)T}{p_mD_m}\right)^{q-1}}{\left((2cq+\Omega)\left(1+\frac{2tcp_1G_{\mathrm{t}}G_{\mathrm{r}}\zeta(\beta-\delta)T}{p_mD_m}\right)-\Omega\right)^q}\frac{\theta}{2\pi}\right.\right. \\ &\left.\left.+\frac{(2cq)^q\left(1+\frac{2tcp_2g_{\mathrm{t}}G_{\mathrm{r}}\zeta(\beta-\delta)T}{p_mD_m}\right)^{q-1}}{\left((2cq+\Omega)\left(1+\frac{2tcp_2g_{\mathrm{t}}G_{\mathrm{r}}\zeta(\beta-\delta)T}{p_mD_m}\right)-\Omega\right)^q}\left(1-\frac{\theta}{2\pi}\right)-1\right)\frac{1}{4\pi D_{\min}^3}\right).\end{aligned} \tag{17}$$

specified, the default simulation system parameters detailed in Table III are used. The outcomes obtained from the analytical expressions derived in Section III are labelled as 'Analysis', whilst the Monte Carlo findings are labelled as 'Simulation'.

TABLE III
DEFAULT PARAMETER OF SIMULATION SYSTEM.

Notation	Parameter	Values
d_0	Distance between UAVs and satellite	300km
R_1	Radius of $\mathcal{V}$	10km
$D_{\min}$	Minimum distance of candidate pairs	1km
p_1, p_2	Power of transmitters in A_1 and A_2	20dBW, 19dBW
λ_1	Density of candidate points	10^{-11}
$\mathcal{SR}(c, q, \Omega)$	SR fading model	$\mathcal{SR}(0.158, 1, 0.1)$
α	Path-loss exponent	2
T	SINR threshold	-18dB
σ^2	AWGN's power spectral density	-160dBm/Hz

A. Validation of Outage Probability Performance

To evaluate the accuracy of the analytical OP expression, a series of Monte Carlo simulations are conducted with a total of 50,000 iterations. These simulations are utilized to generate the plots depicting the simulated OP performance of the heterogeneous aerial-to-satellite uplink. The results obtained under various network settings are depicted in Fig. 5 to 9 accordingly, in comparison with their corresponding theoretical OP performance. We observe that the analytical results exhibit a high degree of concordance with the corresponding simulation results, hence bolstering the credibility and soundness of our theoretical investigation presented in Section III.

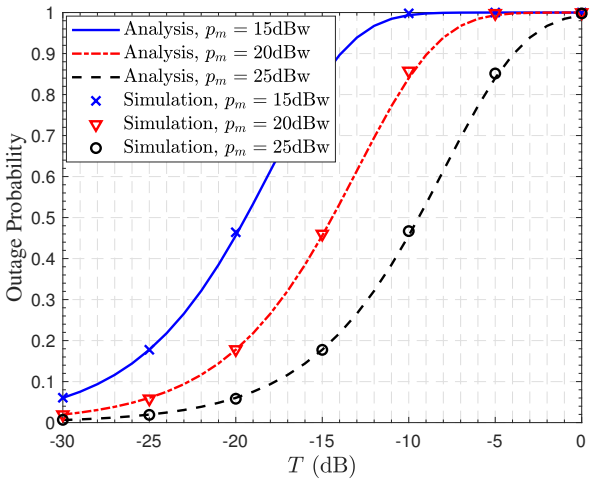

Fig. 5. Outage probability as function of SINR threshold T, given different transmit power p_m of target node.

First Fig. 5 depicts the OP as the function of the SINR threshold T, given three different values of the target node's transmit power p_m. It can be seen from Fig. 5 that as the SINR threshold T[3] increases, the OP, i.e., the likelihood of experiencing the link interruption, also increases. This is due to the inverse relationship between T and the possibility of achieving an SINR that surpasses the given threshold value. Hence, once the threshold value reaches to a specific level, the likelihood of disruption occurring in the link between the aerial transmitter and the satellite reaches its maximum value of 1. Furthermore, increasing the power of the target transmitter leads to an increase in its SINR and this reduces the risk of communication interruption. Therefore, with an increase in p_m, the OP curve exhibits a rightward shift.

[3]In this analysis, the SINR threshold is examined over a range of -30 dB to 0 dB to investigate system behavior under varying link budget conditions. It is worth noting that this threshold is not rigidly defined and can be adapted according to system parameters and specific deployment requirements. Factors such as link budget constraints, signal propagation properties, and the environmental characteristics of the proposed system influence the selection of this threshold. Consequently, the value of the SINR threshold can be adjusted to align with the realistic conditions of different scenarios. Besides, the same principle applies to other parameters as well.

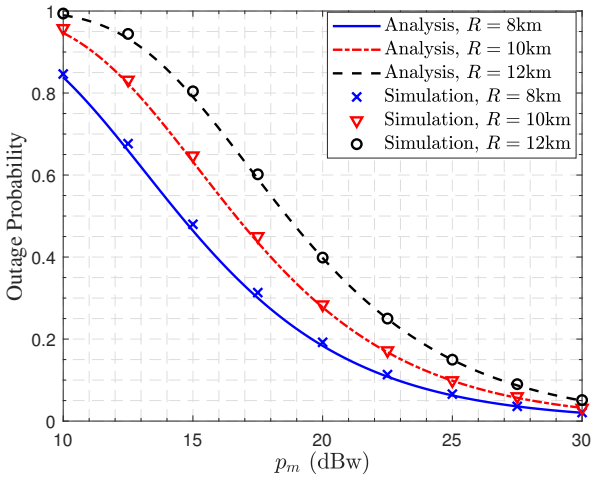

Fig. 6. Outage probability as function of target node transmit power p_m, given different values of spherical space's radius R_1.

Next Fig. 6 plots the OP as the function of p_m, given three different values for the radius R_1 of the spherical space $\mathcal{V}$. As expected, increasing p_m decreases the OP. Also it can be seen that the expansion of the distribution space of aerial transmitters leads to a noticeably worse OP performance. This is because the increased availability of space for the MHCCP deployment of air nodes results in a higher number of transmitters concurrently attempting to access the satellite, leading to a higher MUI and consequently a worsen OP performance.

Then we investigate the impact of node density on the OP, and Fig. 7(a) depicts the OP as the function of p_m, given four different values for the density of candidate points λ_1. As expected, increasing λ_1 increases number of nodes, which results in greater MUI and consequently increases the OP, i.e., the likelihood of communication interruption. However, as can be seen from Fig. 7(a), when λ_1 increases beyond 10^{-9}, the OP appears saturated. This is because the imposed minimum spacing $D_{\min}$ prevents the number of nodes from infinitely escalating as the density increases. To gain a deeper understanding of the limit value of node density under the MHCCP and its influence on the OP, additional simulations are performed as depicted in Fig. 7(b), which demonstrates a clear relationship between increasing λ_1 and the convergence of the OP towards its limit value. This convergence occurs at the limit of λ_3, i.e., $\lim_{\lambda_1 \to \infty} \lambda_3 = \frac{3\bar{c}}{4\pi D_{\min}^3}$, as predicted in **Remark 1**. This finding implies that there exists a maximum number of nodes and the upper bound of OP.

Fig. 8 investigates the influence of the transmission distance

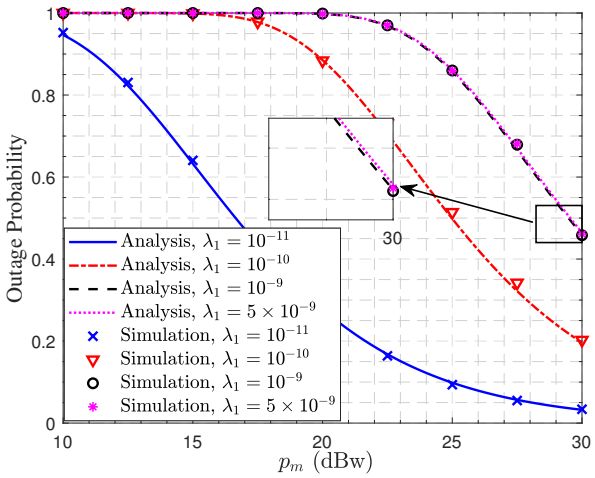

(a)

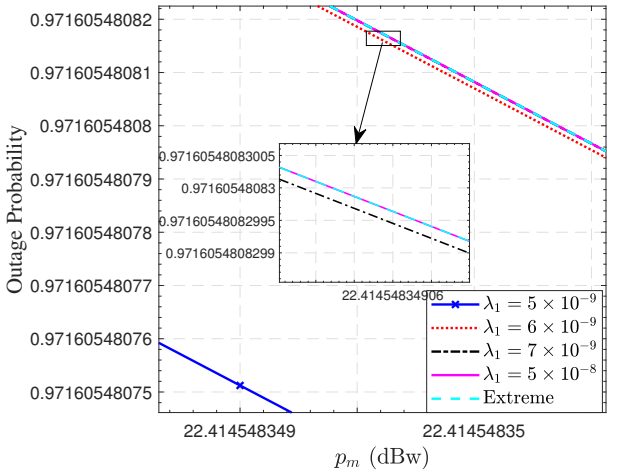

(b)

Fig. 7. Outage probability as function of target node transmit power p_m, given different values for density of candidate points λ_1.

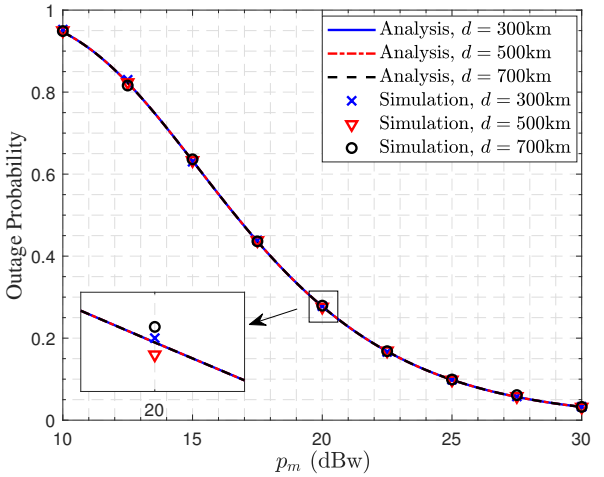

Fig. 8. Outage probability as function of target node transmit power p_m, given different aerial-to-satellite link distances d_0.

of the uplink on the OP, which suggests that changing the transmission distance d_0 of aerial-to-satellite links does not impact on the OP. More specifically, the theoretical OP curves

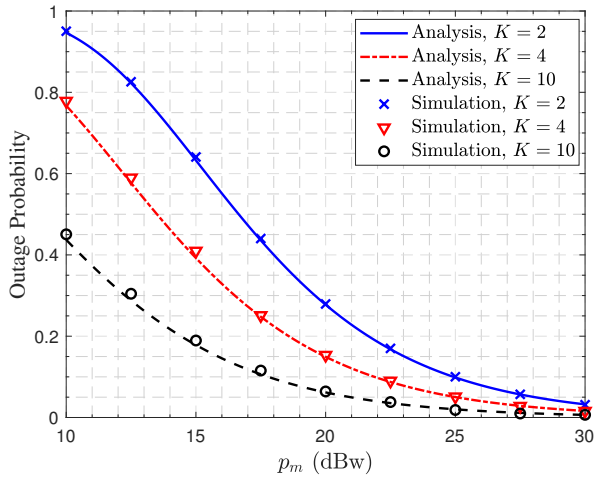

Fig. 9. Outage probability as function of target node transmit power p_m, given different numbers of frequency channels K.

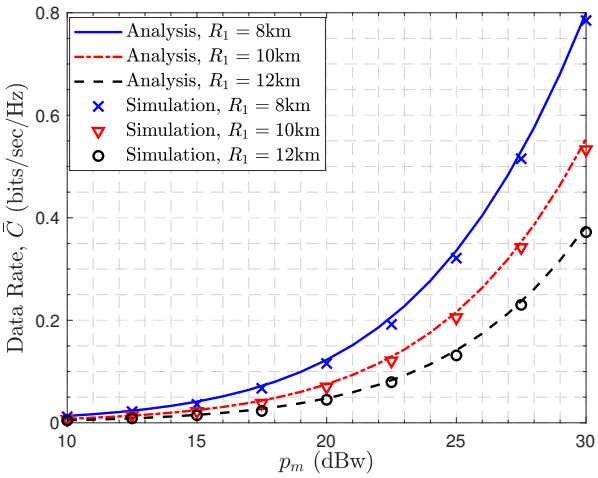

Fig. 10. Average ergodic rate as function of target node transmit power p_m, given different values of spherical space's radius R_1.

corresponding to the three different d_0 coincides, while the simulated OP curves for the three different d_0 are almost the same. This is because changing d_0 changes the desired target node's power and the interference power almost equally, and consequently, the link's SINR does not change.

Fig. 9 provides a clear visual representation of the influence of the number of frequency channels K on the OP, indicating that increasing K decreases the OP. Evidently, providing more frequency channels enables more transmitters operate in orthogonal access mode, thereby resulting in a reduction of the interference towards the intended transmitter. Consequently, the SINR of the target link increases, diminishing the likelihood of interruption.

B. Validation of Average Ergodic Rate Performance

Similarly, Monte Carlo simulations are employed to validate the close-form analytical AER provided by **Theorem 2**. The results obtained are presented in Figs. 10, 11 and 12, which confirm that Monte Carlo simulated data rate closely matches the theoretical AER.

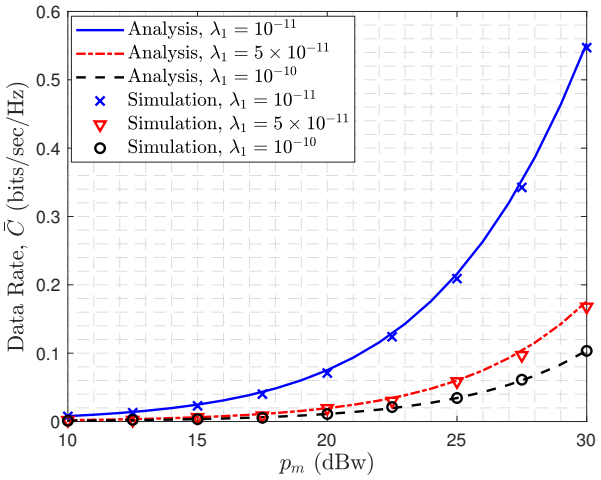

Fig. 11. Average ergodic rate as function of target node transmit power p_m, given different values for density of candidate points λ_1.

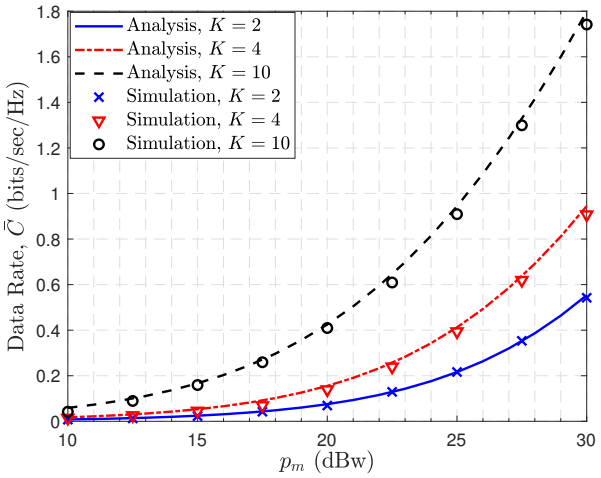

Fig. 12. Average ergodic rate as function of target node transmit power p_m, given different numbers of frequency channels K.

More specifically, Fig. 10 depicts the AER as the function of the target node's transmit power p_m, given three different values for the radius R_1 of the spherical space $\mathcal{V}$. As expected, increasing p_m increases $\bar{C}$. In addition, the impact of R_1 on the achievable AER is clearly shown in Fig. 10. Evidently, increasing the available space $\mathcal{V}$ results in a reduction of the AER, because there are more interference transmitters. Observe that Fig. 10 is consistent with Fig. 6, which is to be expected given the relationship between the OP and AER.

Fig. 11 further investigates the impact of node density on the achievable AER. As expected, increasing λ_1 reduces the AER, since increasing λ_1 leads to more interfering nodes. Obviously, Fig. 11 is entirely consistent with Fig. 7(a), because a higher OP corresponds to a lower AER and vice versus.

Fig. 12 demonstrates the impact of the number of available frequency channels K on the data transmission rate of the uplink. As explained for Fig. 9, an increase in the number of frequency channels K reduces the number of aerial transmitters operating at a same subchannel. This improves the SINR of the uplink, and consequently the data rate is enhanced.

V. Conclusions

In this paper, we have proposed a tractable approach for analyzing the outage probability and average ergodic rate for the uplink of heterogeneous NTNs. Our novel contribution has been three-fold. First, we proposed modeling heterogeneous NTNs using a combination of a Matérn hard-core cluster process and a binomial point process. Second, we derived accurate closed-form expressions for the outage probability and average ergodic rate of the aerial-to-satellite uplink, accounting for realistic multi-user interference and shadowed-Rician channel fading. Third, we calculated and analyzed the upper bound on the density of the MHCCP, providing a precise quantitative benchmark for designing practical models to achieve optimal resource utilization. The accuracy of these theoretical derivations has been extensively validated through Monte Carlo simulations. The closed-form expression for OP, in particular, serves as a robust tool for evaluating the impact of various configurations on link performance, facilitating the optimization of deployment strategies, power control schemes, and satellite resource allocation for UAV groups. This is crucial for improving system efficiency and minimizing the risk of communication interruptions. By incorporating heterogeneous low-altitude UAV groups into the model, the closed-form solution can reveal how different types of UAVs (they may differ, e.g., in terms of density, power, antenna gain, etc.) contribute to the overall OP and AER. This insight provides a theoretical foundation for optimizing links in scenarios involving diverse UAV collaborations.

Appendix

A. Proof of Theorem 1

Proof. Using the Kummer's transform of the hypergeometric function [37], we can rewrite the PDF of $|h|^2$ as $f_{|h|^2}(x) = \sum_{k=0}^{\infty} \Psi(k) x^k \exp(-(\beta-\delta)x$, where $\Psi(k) = \frac{(-1)^k \kappa \delta^k}{(k!)^2} \mathrm{Ps}(1-q)_k$. Then, the CDF of $|h|^2$ can be represented as

$$F_{|h|^2}(x) = \sum_{k=0}^{\infty} \Psi(k) \int_0^x t^k \exp(-(\beta-\delta)t) \mathrm{d}t$$
$$= \sum_{k=0}^{\infty} \frac{\Psi(k)}{(\beta-\delta)^{k+1}} \gamma(k+1, (\beta-\delta)x). \quad (20)$$

Therefore, we can obtain $P_{\rm out}$ as

$$\begin{aligned}
P_{\rm out} &\triangleq \mathbb{P}\left(\frac{p_m D_m |h_m|^2 d_m^{-\alpha}}{I+\sigma^2} \le T\right) \\
&= \mathbb{P}\left(|h_m|^2 \le \frac{T(I+\sigma^2)d_m^{\alpha}}{p_m D_m}\right) \\
&= \mathbb{E}\left[\kappa \sum_{k=0}^{\infty} \frac{\Psi(k)}{(\beta-\delta)^{k+1}} \gamma\left(k+1, (\beta-\delta)\frac{T(I+\sigma^2)d_m^{\alpha}}{p_m D_m}\right)\right] \\
&\overset{(a)}{\approx} \mathbb{E}\Bigg[\sum_{k=0}^{\infty} \frac{\Psi(k)}{(\beta-\delta)^{k+1}} \Gamma(k+1) \\
&\quad \times \left(1-\exp\left(-\frac{\zeta(\beta-\delta)T(I+\sigma^2)d_m^{\alpha}}{p_m D_m}\right)\right)^{k+1}\Bigg] \\
&\overset{(b)}{=} \sum_{k=0}^{\infty} \frac{\Psi(k)}{(\beta-\delta)^{k+1}} \Gamma(k+1) \sum_{t=0}^{k+1} \binom{k+1}{t} (-1)^t \\
&\quad \times \mathbb{E}\left[\exp(-s(I+\sigma^2))\right], \qquad (21)
\end{aligned}$$

where (a) is approximated by using $\gamma(k+1,x) < \Gamma(k+1)(1-\exp(-\zeta x))^{k+1}$ [38], $\zeta = (\Gamma(k+2))^{-\frac{1}{k+1}}$, and (b) is obtained from the binomial theorem [39] with $s = \frac{t\zeta(\beta-\delta)Td_m^{\alpha}}{p_m D_m}$. This completes the proof. □

B. Proof of Lemma 1

Proof.

$$\begin{aligned}
\mathcal{L}_I(s) &= \mathbb{E}\left[\exp(-sI)\right] \\
&= \mathbb{E}\left[\exp\Big(-s\sum_{l\in\{1,2\}}\sum_{x_l\in\phi_l\setminus\{m\}} p_l D_{x_l} |h_{x_l}|^2 d_{x_l}^{-\alpha}\Big)\right]. \qquad (22)
\end{aligned}$$

As the point process and the fading process are independent of each other, $\mathcal{L}_I(s)$ can be expressed as

$$\begin{aligned}
\mathcal{L}_I(s) &= \mathbb{E}\left[\prod_{l\in\{1,2\}}\prod_{x_l\in\phi_l\setminus\{m\}} \mathbb{E}_{|h_{x_l}|^2}\Big[\exp\Big(-sp_l D_{x_l}|h_{x_l}|^2 d_{x_l}^{-\alpha}\Big)\Big]\right] \\
&\overset{(a)}{=} \mathbb{E}_{N_l}\left[\prod_{l\in\{1,2\}}\prod_{x_l\in\phi_l\setminus\{m\}} \mathbb{E}_{D_{x_l},|h_{x_l}|^2}\Big[\exp\left(-t_l|h_{x_l}|^2\right)\Big]\right], \qquad (23)
\end{aligned}$$

where (a) is obtained by assuming that all the aerial transmitters have the same transmission distance and denoting $t_l = sp_l D_{x_l} d_0^{-\alpha}$.

As shown in [33], the moment-generating function of the SR model is defined as $M_S(x) = \mathbb{E}\left[\exp(-xS)\right] = \frac{(2cq)^q(1+2cx)^{q-1}}{((2cq+\Omega)(1+2cx)-\Omega)^q}$. Thus, we further obtain

$$\begin{aligned}
\mathcal{L}_I(s) &= \mathbb{E}_{N_l}\Bigg[\prod_{l\in\{1,2\}}\prod_{x_l\in\phi_l\setminus\{m\}} \mathbb{E}_{D_{x_l}}\Big[\underbrace{\frac{(2cq)^q(1+2ct_l)^{q-1}}{((2cq+\Omega)(1+2ct_l)-\Omega)^q}}_{M_1(t_l)}\Big]\Bigg] \\
&\overset{(b)}{=} \mathbb{E}_{N_l}\Bigg[\prod_{l\in\{1,2\}}\prod_{x_l\in\phi_l\setminus\{m\}} \Big[\underbrace{M_1(\mu_l)\frac{\theta}{2\pi} + M_1(\nu_l)\Big(1-\frac{\theta}{2\pi}\Big)}_{M_2(l)}\Big]\Bigg] \\
&= \mathbb{E}_{N_1}\Bigg[\prod_{x_1\in\phi_1\setminus\{m\}} M_2(1)\Bigg]\mathbb{E}_{N_2}\Bigg[\prod_{x_2\in\phi_2\setminus\{m\}} M_2(2)\Bigg] \\
&\overset{(c)}{=} \sum_{n=1}^{n_1}\binom{n_1}{n} P_I^n (1-P_I)^{n_1-n} \left(M_2(1)\right)^n \\
&\quad \times \sum_{n_2=0}^{\infty} \frac{(\lambda_3 V_1)^{n_2}}{n_2!} \exp(-\lambda_3 V_1)(M_2(2))^{n_2} \\
&\overset{(d)}{=} (M_2(1))^{n_1} \exp\left(\lambda_3 V_1 (M_2(2)-1)\right), \qquad (24)
\end{aligned}$$

where (b) is obtained by denoting $\mu_l = sp_l d_0^{-\alpha} G_{\rm t} G_{\rm r}$ and $\nu_l = sp_l d_0^{-\alpha} g_{\rm t} G_{\rm r}$, (c) is obtained by the fact that Φ_{A_1} follows the BPP with P_I being the proportion of the interfering nodes to the total number of nodes in Φ_{A_1}, Φ_{A_2} follows the PPP with the density of λ_3 and the volume of the spherical space $\mathcal{V}$ is $V_1 = \frac{4\pi R_1^3}{3}$, and (d) is obtained by the fact that all the nodes in Φ_{A_1} are interference nodes and hence $P_I = 1$. This completes the proof. □

C. Proof of Theorem 2

Proof. From the definition (18), we have

$$\begin{aligned}
\bar{C} &\triangleq \mathbb{E}_{h_m,d_m,I}\left[\log_2(1+\mathrm{SINR})\right] \\
&\overset{(a)}{=} \mathbb{E}_{h_m,d_m,I}\left[\int_{t>0} \mathbb{P}\Big(\log_2(1+\frac{p_m D_m |h_m|^2 d_m^{-\alpha}}{I+\sigma^2}) > t\Big)\mathrm{d}t\right] \\
&= \mathbb{E}_{h_m,d_m,I}\left[\int_{t>0} \mathbb{P}\Big(|h_m|^2 > \frac{d_m(I+\sigma^2)}{p_m D_m}(2^t-1)\Big)\mathrm{d}t\right], \qquad (25)
\end{aligned}$$

where (a) follows form the fact that the random variable involved is positive. Then, we have

$$\begin{aligned}
\bar{C} &\overset{(b)}{=} \mathbb{E}_I\left[\int_{t>0}\left(1-F_{|h_m|^2}\left(\frac{d_m(I+\sigma^2)(2^t-1)}{p_m D_m}\right)\right)\mathrm{d}t\right] \\
&= \mathbb{E}_I\Bigg[\int_{t>0}\Bigg(1-\kappa\sum_{k=0}^{\infty}\frac{\Psi(k)}{(\beta-\delta)^{k+1}}\gamma\big(k+1,(\beta-\delta)\big) \\
&\quad \times \frac{(2^t-1)(I^2+\sigma^2)d_m^{\alpha}}{p_m D_m}\Bigg)\mathrm{d}t\Bigg] \\
&\overset{(c)}{\approx} \mathbb{E}_I\Bigg[\int_{t>0}\Bigg(1-\sum_{k=0}^{\infty}\frac{\Psi(k)}{(\beta-\delta)^{k+1}}\Gamma(k+1) \\
&\quad \times \left(1-\exp\Big(-\frac{\zeta(\beta-\delta)(2^t-1)(I+\sigma^2)d_m^{\alpha}}{p_m D_m}\Big)\right)^{k+1}\Bigg)\mathrm{d}t\Bigg] \\
&\overset{(d)}{=} \int_{t>0}\Bigg(1-\sum_{k=0}^{\infty}\frac{\Psi(k)}{(\beta-\delta)^{k+1}}\Gamma(k+1) \\
&\quad \times \sum_{j=0}^{k+1}\binom{k+1}{j}(-1)^j \mathbb{E}_I\left[\exp(-s(I+\sigma^2))\right]\Bigg)\mathrm{d}t \\
&= \int_{t>0}\Bigg(1-\sum_{k=0}^{\infty}\frac{\Psi(k)}{(\beta-\delta)^{k+1}}\Gamma(k+1) \\
&\quad \times \sum_{j=0}^{k+1}\binom{k+1}{j}(-1)^j \exp(-s\sigma^2)\mathcal{L}_I(s)\Bigg)\mathrm{d}t, \qquad (26)
\end{aligned}$$

where (b) is obtained from (20), (c) is approximated by using $\gamma(k+1,x) < \Gamma(k+1)(1-exp(-\zeta x))^{k+1}$ [38], $\zeta = (\Gamma(k+2))^{-\frac{1}{k+1}}$, and (d) is obtained from the binomial theorem with $s = \frac{j\zeta(\beta-\delta)(2^t-1)d_m^{\alpha}}{p_m D_m}$. Substituting $\mathcal{L}_I(s)$ of (11) into (26) leads to (19). This completes the proof. □

REFERENCES

[1] M. M. Azari, *et al.*, "Evolution of non-terrestrial networks from 5G to 6G: A survey," *IEEE Commun. Surveys & Tuts.*, vol. 24, no. 4, pp. 2633–2672, 4th Quart. 2022.

[2] D. Hu, *et al.*, "A cyber–physical routing protocol exploiting trajectory dynamics for mission-oriented flying ad hoc networks," *Engineering*, vol. 19, pp. 217–227, Dec. 2022.

[3] J. Y. Chen, "UAV-guided navigation for ground robot teleoperation in a military reconnaissance environment," *Ergonomics*, vol. 53, no. 8, pp. 940–950, Jul. 2010.

[4] M. A. Ma'Sum, *et al.*, "Simulation of intelligent unmanned aerial vehicle (UAV) for military surveillance," in *Proc. ICACSIS 2013* (Sanur Bali, Indonesia), Sep. 28-29, 2013, pp. 161–166.

[5] S. N. Chiu, D. Stoyan, W. S. Kendall, and J. Mecke, *Stochastic Geometry and Its Applications* (3rd Edition). John Wiley & Sons, 2013.

[6] J. Dall and M. Christensen, "Random geometric graphs," *Phys. Rev. E*, vol. 66, no. 1, pp. 16121–16121, Jul. 2002.

[7] N. Okati, *et al.*, "Downlink coverage and rate analysis of low earth orbit satellite constellations using stochastic geometry," *IEEE Trans. Commun.*, vol. 68, no. 8, pp. 5120–5134, Aug. 2020.

[8] A. Yastrebova, *et al.*, "Theoretical and simulation-based analysis of terrestrial interference to LEO satellite uplinks," in *Proc. GLOBECOM 2020* (Taipei, Taiwan, China), Dec. 7-11, 2020, pp. 1–6.

[9] X. Zhang, *et al.*, "Stochastic geometry-based analysis of cache-enabled hybrid satellite-aerial-terrestrial networks with non-orthogonal multiple access," *IEEE Trans. Wireless Commun.*, vol. 21, no. 2, pp. 1272–1287, Feb. 2022.

[10] Z. Song, *et al.*, "Cooperative satellite-aerial-terrestrial systems: A stochastic geometry model," *IEEE Trans. Wireless Commun.*, vol. 22, no. 1, pp. 220–236, Jan. 2023.

[11] Y. Liu, *et al.*, "Space-air-ground integrated networks: Spherical stochastic geometry-based uplink connectivity analysis," *IEEE J. Sel. Areas Commun.*, vol. 42, no. 5, pp. 1387–1402, May. 2024.

[12] B. Al Homssi and A. Al-Hourani, "Modeling uplink coverage performance in hybrid satellite-terrestrial networks," *IEEE Commun. Lett.*, vol. 25, no. 10, pp. 3239–3243, Oct. 2021.

[13] A. Talgat, M. A. Kishk, and M. S. Alouini, "Stochastic geometry-based analysis of LEO satellite communication systems," *IEEE Commun. Lett.*, vol. 25, no. 8, pp. 2458–2462, Aug. 2021.

[14] A. Al-Hourani, "An analytic approach for modeling the coverage performance of dense satellite networks," *IEEE Wireless Commun. Lett.*, vol. 10, no. 4, pp. 897–901, Apr. 2021.

[15] N. Okati and T. Riihonen, "Modeling and analysis of LEO mega-constellations as nonhomogeneous Poisson point processes," in *Proc. VTC-Spring 2021* (Helsinki, Finland), Apr. 25-28, 2021, pp. 1–5.

[16] R. Wang, M. A. Kishk, and M.-S. Alouini, "Evaluating the accuracy of stochastic geometry based models for LEO satellite networks analysis," *IEEE Commun. Lett.*, vol. 26, no. 10, pp. 2440–2444, Oct. 2022.

[17] H. Zhang, *et al.*, "Outage analysis of cooperative satellite-aerial-terrestrial networks with spatially random terminals," *IEEE Trans. Commun.*, vol. 70, no. 7, pp. 4972–4987, Jul. 2022.

[18] A. Talgat, M. A. Kishk and M.-S. Alouini, "Nearest neighbor and contact distance distribution for binomial point process on spherical surfaces," *IEEE Commun. Lett.*, vol. 24, no. 12, pp. 2659-2663, Dec. 2020.

[19] J. G. Andrews, A. K. Gupta, and H. S. Dhillon, "A primer on cellular network analysis using stochastic geometry," Oct. 2016, *arXiv:1604.03183.* [Online]. Available: http://arxiv.org/abs/1604.03183

[20] S. Srinivasa and M. Haenggi, "Distance distributions in finite uniformly random networks: Theory and applications," *IEEE Trans. Veh. Technol.*, vol. 59, no. 2, pp. 940–949, Feb. 2010.

[21] Y. J. Chun, M. O. Hasna, and A. Ghrayeb, "Modeling heterogeneous cellular networks interference using Poisson cluster processes," *IEEE J. Sel. Areas Commun.*, vol. 33, no. 10, pp. 2182-2195, Oct. 2015.

[22] B. Cho, K. Koufos, and R. Jantti, "Bounding the mean interference in Matérn type ii hard-core wireless networks," *IEEE Wireless Commun. Lett.*, vol. 2, no. 5, pp. 563–566, Oct. 2013.

[23] C. Loo, "A statistical model for a land mobile satellite link," *IEEE Trans. Veh. Technol.*, vol. 34, no. 3, pp. 122–127, Aug. 1985.

[24] D.-H. Jung, J.-G. Ryu, W.-J. Byun, and J. Choi, "Performance analysis of satellite communication system under the shadowed-Rician fading: A stochastic geometry approach," *IEEE Trans. Commun.*, vol. 70, no. 4, pp. 2707–2721, Apr. 2022.

[25] B. Al Homssi and A. Al-Hourani, "Optimal beamwidth and altitude for maximal uplink coverage in satellite networks," *IEEE Wireless Commun. Lett.*, vol. 11, no. 4, pp. 771-775, Apr. 2022.

[26] H. Jia, C. Jiang, L. Kuang and J. Lu, "An analytic approach for modeling uplink performance of mega constellations," *IEEE Trans. Veh. Technol.*, vol. 72, no. 2, pp. 2258-2268, Feb. 2023.

[27] M. Sellathurai, S. Vuppala, and T. Ratnarajah, "User selection for multi-beam satellite channels: A stochastic geometry perspective," in *Proc. 50th Asilomar Conf. Signals, Syst. Comput.* (Pacific Grove, CA, USA), Nov. 6-9, 2016, pp. 487–491.

[28] O. Y. Kolawole, S. Vuppala, M. Sellathurai, and T. Ratnarajah, "On the performance of cognitive satellite-terrestrial networks," *IEEE Trans. Cogn. Commun. Netw*, vol. 3, no. 4, pp. 668–683, Dec. 2017.

[29] A. Talgat, M. A. Kishk and M.-S. Alouini, "Stochastic geometry-based uplink performance analysis of IoT over LEO satellite communication," *IEEE Trans. Aerosp. Electron. Syst.*, vol. 60, no. 4, pp. 4198-4213, Aug. 2024.

[30] W.-Y. Dong, S. Yang, W. Lin, W. Zhao, J.-X. Gui, and S. Chen, "Outage probability analysis of uplink heterogeneous non-terrestrial networks: A novel stochastic geometry model," in *Proc. GLOBECOM 2024* (Cape Town, South Africa), Dec. 8-12, 2024, pp. 2588-2593.

[31] M. Arti, "Two-way satellite relaying with estimated channel gains," *IEEE Trans. Commun.*, vol. 64, no. 7, pp. 2808–2820, Jul. 2016.

[32] K. Guo, *et al.*, "Performance analysis of hybrid satellite-terrestrial cooperative networks with relay selection," *IEEE Trans. Veh. Technol.*, vol. 69, no. 8, pp. 9053–9067, Aug. 2020.

[33] A. Abdi, W. C. Lau, M.-S. Alouini, and M. Kaveh, "A new simple model for land mobile satellite channels: First- and second-order statistics," *IEEE Trans. Commun.*, vol. 2, no. 3, pp. 519–528, May 2003.

[34] M. R. Bhatnagar and M. Arti, "On the closed-form performance analysis of maximal ratio combining in shadowed-Rician fading LMS channels," *IEEE Commun. Lett.*, vol. 18, no. 1, pp. 54–57, Jan. 2014.

[35] D.-H. Jung and D.-G. Oh, "Outage performance of shared-band on-board processing satellite communication system," in *Proc. VTC-Fall 2018* (Chicago, IL, USA), Aug. 27-30, 2018, pp. 1–5.

[36] X. Zhang, *et al.*, "Performance analysis of NOMA-based cooperative spectrum sharing in hybrid satellite-terrestrial networks," *IEEE Access*, vol. 7, pp. 172321–172329, Dec. 2019.

[37] L. Fructos, R. R. Boix, and F. Mesa, "Application of Kummer's transformation to the efficient computation of the 3-D green's function with 1-D periodicity," *IEEE Trans. Antennas Propag.*, vol. 58, no. 1, pp. 95–106, Jan. 2010.

[38] H. Alzer, "On some inequalities for the incomplete gamma function," *Math. Comput.*, vol. 66, no. 218, pp. 771–778, 1997.

[39] E. W. Weisstein, "Binomial theorem," Wolfram MathWorld, 2002. https://mathworld.wolfram.com/BinomialTheorem.html

Wen-Yu Dong (Student Member, IEEE) received the B.S. degree in electronic and information engineering from Sichuan University (SCU), China, in 2019. He is currently pursuing the Ph.D. degree in information and communication engineering with the School of Information and Communication Engineering, Beijing University of Posts and Telecommunications (BUPT), and the Key Laboratory of Universal Wireless Communications, Ministry of Education. His current research interests include highly dynamic mobile ad hoc network architecture and protocol stack design, routing design for mobile ad hoc networks, and integrated space-air-ground network modeling and performance analysis based on stochastic geometry.

Shaoshi Yang (Senior Member, IEEE) received the B.Eng. degree in information engineering from Beijing University of Posts and Telecommunications (BUPT), China, in 2006, and the Ph.D. degree in electronics and electrical engineering from the University of Southampton, U.K., in 2013. From 2008 to 2009, he was a Researcher with Intel Labs China. From 2013 to 2016, he was a Research Fellow with the School of Electronics and Computer Science, University of Southampton. From 2016 to 2018, he was a Principal Engineer with Huawei Technologies Co. Ltd., where he made significant contributions to the products, solutions, and standardization of 5G, wideband IoT, and cloud gaming/VR. He was a Guest Researcher with the Isaac Newton Institute for Mathematical Sciences, University of Cambridge. He is currently a Full Professor with BUPT. His research interests include 5G/5G-A/6G, massive MIMO, mobile ad hoc networks, distributed artificial intelligence, and cloud gaming/VR. He is a Standing Committee Member of the CCF Technical Committee on Distributed Computing and Systems. He received the Dean's Award for Early Career Research Excellence from the University of Southampton in 2015, the Huawei President Award for Wireless Innovations in 2018, the IEEE TCGCC Best Journal Paper Award in 2019, the IEEE Communications Society Best Survey Paper Award in 2020, the Xiaomi Young Scholars Award in 2023, the CAI Invention and Entrepreneurship Award in 2023, the CIUR Industry-University-Research Cooperation and Innovation Award in 2023, and the First Prize of Beijing Municipal Science and Technology Advancement Award in 2023. He is an Editor of *IEEE Transactions on Communications*, *IEEE Transactions on Vehicular Technology*, and *Signal Processing* (Elsevier). He was also an Editor of *IEEE Systems Journal* and *IEEE Wireless Communications Letters*. For more details on his research progress, please refer to https://shaoshiyang.weebly.com/.

Sheng Chen (Life Fellow, IEEE) received the B.Eng. degree in control engineering from East China Petroleum Institute, Dongying, China, in 1982, the Ph.D. degree in control engineering from the City, University of London in 1986, and the Doctor of Sciences (D.Sc.) degree from the University of Southampton, Southampton, U.K., in 2005. From 1986 to 1999, he held research and academic appointments at The University of Sheffield, U.K., The University of Edinburgh, U.K., and the University of Portsmouth, U.K. Since 1999, he has been with the School of Electronics and Computer Science, University of Southampton, where he is currently a Professor of intelligent systems and signal processing. He has published over 700 research articles. He has more than 20,000 Web of Science citations with an H-index of 63 and more than 40,000 Google Scholar citations with an H-index of 85. His research interests include adaptive signal processing, wireless communications, modeling and identification of nonlinear systems, neural network and machine learning, evolutionary computation methods, and optimization. He is a Fellow of the Royal Academy of Engineering, U.K., a Fellow of Asia–Pacific Artificial Intelligence Association, and a Fellow of IET. He was one of the original ISI Highly Cited Researchers in Engineering in March 2004.